




Merging of transport theory with the time-dependent Hartree-Fock approach: Multinucleon transfer in U+U collisions

S. Ayik ^{1,*}, B. Yilmaz ², O. Yilmaz,³ and A. S. Umar ⁴

¹Physics Department, Tennessee Technological University, Cookeville, Tennessee 38505, USA

²Physics Department, Faculty of Science, Ankara University, 06100, Ankara, Turkey

³Physics Department, Middle East Technical University, 06800, Ankara, Turkey

⁴Department of Physics and Astronomy, Vanderbilt University, Nashville, Tennessee 37235, USA



(Received 29 June 2020; revised 25 July 2020; accepted 3 August 2020; published 17 August 2020)

Multinucleon transfer mechanism in the collision of $^{238}\text{U} + ^{238}\text{U}$ system is investigated at $E_{c.m.} = 833$ MeV in the framework of the quantal diffusion description based on the stochastic mean-field approach. Double cross sections $\sigma(N, Z)$ as a function of the neutron and proton numbers, the cross sections $\sigma(Z)$ and $\sigma(A)$ as a function of the atomic numbers and the mass numbers are calculated for production of the primary fragments. The calculation indicates the $^{238}\text{U} + ^{238}\text{U}$ system may be located at an unstable equilibrium state at the potential energy surface with a slightly negative curvature along the β stability line on the (N, Z) plane. This behavior may lead to rather large diffusion along the β stability direction.

DOI: [10.1103/PhysRevC.102.024619](https://doi.org/10.1103/PhysRevC.102.024619)

I. INTRODUCTION

It has been recognized that multinucleon transfer in heavy-ion collisions involving massive nuclei provide a suitable mechanism for synthesizing new neutron-rich heavy nuclei [1–14]. For this purpose, experimental investigations have been carried out in heavy-ion collisions with actinide targets near barrier energies [15–18]. Collisions of massive systems near barrier energies predominantly lead to dissipative deep-inelastic reactions and quasifission reactions. In dissipative collisions the most part of the bombarding energy is converted into the internal excitations, and the multinucleon transfer occurs between the projectile and target nuclei. A number of experimental and theoretical investigations have been made of the multinucleon transfer mechanism in heavy-ion collisions near barrier energies. The multidimensional phenomenological Langevin-type dynamical approaches have been developed for describing dissipative collisions between massive nuclear systems [13, 19–22]. These phenomenological models provide a qualitative and in some cases semiquantitative description of the transfer process. For many years, the time-dependent Hartree-Fock (TDHF) approach has been used for describing the deep-inelastic collisions and the quasifission reactions [11, 23–28]. The TDHF provides a microscopic description in terms of Skyrme-type energy density functionals. The mean-field theory provides a good description for the most probable dynamical path of the collective motion at low-energy heavy-ion collisions including the one-body dissipation mechanism. However, the mean-field theory severely underestimates the fluctuations around the most probable collective path. The particle number projection method of the TDHF indeed shows

the fragment mass and charge distributions are largely underestimated for strongly damped collisions [8, 29]. The fragment mass and charge distributions observed in symmetric collisions provide a good example for the shortcoming of the mean-field description. In the TDHF calculations of the symmetric collisions, the identities of the projectile and target are strictly preserved, i.e., the mass and charge numbers of the final fragments are exactly same as of those at the initial fragments. The experiments, on the other hand, exhibit broad mass and charge distributions of final fragments around their initial values. The dominant aspect of the data is a broad mass and charge distribution around the projectile and target resulting from multinucleon diffusion mechanism. The description of such large fluctuations requires an approach beyond the mean-field theory. The time-dependent RPA approach of Balian and Veneroni provides a possible approach for calculating dispersion of fragment mass and charge distributions and dispersion of other one-body observables [30–34]. However, this approach has severe technical difficulties in applications to the collisions of asymmetric systems. In this work, we employ the quantal diffusion description based on the stochastic mean-field (SMF) approach to calculate double cross sections $\sigma(N, Z)$, the cross section as function of mass number $\sigma(A)$, and cross section as a function of the atomic number $\sigma(Z)$ of the primary fragments in the collisions of the symmetric $^{238}\text{U} + ^{238}\text{U}$ system at $E_{c.m.} = 833$ MeV [35, 36]. In the quantal diffusion description, the transport theoretical concepts are merged with the mean-field description of the TDHF. As a result, it is possible to calculate the transport coefficients of macroscopic variables in terms of the mean-field properties provided by the time-dependent wave functions of the TDHF, which is consistent with the fluctuation-dissipation theorem of the nonequilibrium statistical mechanics. In Sec. II, we present a brief description of the quantal nucleon diffusion

* ayik@tntech.edu

description of the multinucleon exchange. In Sec. III, we present results of calculations of the cross sections for production of the primary fragments, and conclusions are given in Sec. IV. Some calculations details are provided in the Appendixes.

II. QUANTAL DIFFUSION OF MULTINUCLEON TRANSFERS

In the SMF approach, the dynamics of heavy-ion collisions is described in terms of an ensemble of mean-field events. Each event is determined by the self-consistent mean-field Hamiltonian of that event with the initial conditions specified by the thermal and quantal fluctuations at the initial state. We consider uranium-uranium collisions at bombarding energies near Coulomb barrier. During the collision, the projectile and the target form a di-nuclear complex and interact mainly by multinucleon exchanges. Because of the dinuclear structure, rather than generating an ensemble of stochastic mean-field events, it is possible to describe the dynamics in terms of several relevant macroscopic variables, such as neutron and proton numbers of the one side of the complex and relative momentum of projectilelike and the targetlike fragments. It is possible to deduce the Langevin-type transport description for the macroscopic variables [37,38] and calculate transport coefficients of the macroscopic variables in terms of the TDHF solutions. In this manner, the SMF approach provides a ground for merging transport theory with the mean-field description. For the detailed description of the SMF approach and the applications, we refer the reader to the previous publications [39–44]. Here we take the neutron N_1^λ and the proton Z_1^λ numbers of the projectilelike fragments as the macroscopic variables. In each event λ , the neutron and proton numbers are determined by integrating the nucleon density over the projectile side of the window between the colliding nuclei,

$$\left(N_1^\lambda(t)\right) = \int d^3r \Theta[x'(t)] \left(\rho_n^\lambda(\vec{r}, t) \right), \quad (1)$$

where $x'(t) = [y - y_0(t)] \sin \theta + [x - x_0(t)] \cos \theta$. The (x, y) plane represents the reaction plane with x axis being the beam direction in the center-of-mass (COM) frame of the colliding ions. The window plane is perpendicular to the symmetry axis and its orientation is specified by the condition $x'(t) = 0$. In this expression, $x_0(t)$ and $y_0(t)$ denote the coordinates of the window center relative to the origin of the COM frame, $\theta(t)$ is the smaller angle between the orientation of the symmetry axis and the beam direction. We neglect fluctuations in the orientation of the window and determine the mean evolution of the window dynamics by diagonalizing the mass quadrupole moment of the system for each impact parameter b or the initial orbital angular momentum ℓ , as described in Appendix A, of Ref. [40]. In terms of the TDHF description, it is possible to determine time evolution of the rotation angle $\theta(t)$ of the symmetry axis. The coordinates $x_0(t)$ and $y_0(t)$ of the center point of the window are located at the center of the minimum density slice on the neck between the colliding ions. Since uranium is a deformed nucleus, the outcome of the collisions depends on the relative orientation

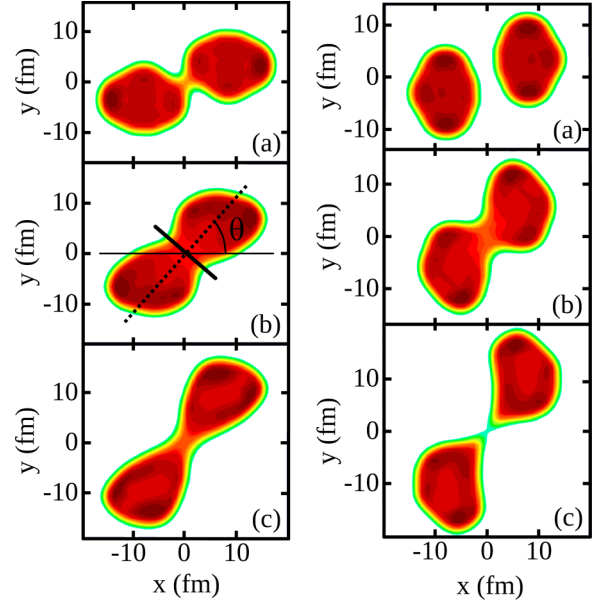


FIG. 1. The density profile and the collision geometry of the $^{238}\text{U} + ^{238}\text{U}$ collisions at $E_{\text{c.m.}} = 833$ MeV with the initial orbital angular momentum $\ell = 300\hbar$ at times $t = 300$ fm/c, $t = 500$ fm/c, and $t = 700$ fm/c at tip-tip geometry (left panel) and side-side geometry (right panel).

of the projectile and target. In the present work, we consider two specific collision geometry: (i) the side-side collisions in which deformation axes of the both the projectile and the target are perpendicular to the beam direction and (ii) the tip-tip is collisions in which deformation axes of the both the projectile and the target are parallel to the beam direction. As an example, Fig. 1 shows the density profile in the tip-tip geometry (left panel) and in the side-side geometry (right panel) of the $^{238}\text{U} + ^{238}\text{U}$ system at $E_{\text{c.m.}} = 833$ MeV with the initial orbital angular momentum $\ell = 300\hbar$ at times $t = 300$ fm/c, $t = 500$ fm/c, and $t = 700$ fm/c. The window plane and symmetry axis of the dinuclear complex are indicated by thick and dashed lines in the left panel of Fig. 1(b). In the calculation of this figure and in the calculations presented in the rest of the paper, we employ the TDHF code developed by Umar *et al.* [45,46] using the SLy4d Skyrme functional [47]. In the following, all quantities are calculated for a given initial orbital angular momentum ℓ , but for the purpose of clarity of expressions, we do not attach the angular momentum label to the quantities. The quantities in Eq. (1)

$$\rho_\alpha^\lambda(\vec{r}, t) = \sum_{ij \in \alpha} \Phi_j^{*\alpha}(\vec{r}, t; \lambda) \rho_{ji}^\lambda \Phi_i^\alpha(\vec{r}, t; \lambda), \quad (2)$$

are the neutron and proton densities in the event λ of the ensemble. Here, and in the rest of the paper, we use the notation $\alpha = n, p$ for the neutron and proton labels. According to the main postulate of the SMF approach, the elements of the initial density matrix are specified by uncorrelated Gaussian distributions with the mean values $\bar{\rho}_{ji}^\lambda = \delta_{ji} n_j$ and the second moments determined by,

$$\overline{\delta \rho_{ji}^\lambda \delta \rho_{i'j'}^\lambda} = \frac{1}{2} \delta_{i'i} \delta_{j'j} [n_i(1 - n_j) + n_j(1 - n_i)], \quad (3)$$

where n_j are the average occupation numbers of the single-particle wave functions at the initial state. At zero initial temperature, these occupation numbers are zero or one, and at finite initial temperatures the occupation numbers are given by the Fermi-Dirac functions. Here and below, the bar over the quantity indicates the average over the generated ensemble.

Below, we briefly discuss the derivation of the Langevin equations for the neutron and proton numbers of the projectilelike fragments, for further details we refer the reader to Refs. [39–42]. The rate of changes the neutron and the proton numbers of the projectilelike fragment are given by,

$$\frac{d}{dt} \begin{pmatrix} N_1^\lambda(t) \\ Z_1^\lambda(t) \end{pmatrix} = - \int d^3r \Theta[x'(t)] \begin{pmatrix} \vec{\nabla} \cdot \vec{j}_n^\lambda(t) \\ \vec{\nabla} \cdot \vec{j}_p^\lambda(t) \end{pmatrix}. \quad (4)$$

In obtaining this expression we neglect a term arising from the rate of change of the position and the rotation of the window plane and employ the continuity equation, with the fluctuating neutron and proton current densities

$$\vec{j}_\alpha^\lambda(\vec{r}, t) = \frac{\hbar}{m} \sum_{ij \in \alpha} \text{Im}(\Phi_j^{*\alpha}(\vec{r}, t; \lambda) \vec{\nabla} \Phi_i^\alpha(\vec{r}, t; \lambda) \rho_{ji}^\lambda). \quad (5)$$

By carrying out a partial integration, we obtain a set of coupled Langevin equations for the macroscopic variables $N_1^\lambda(t)$ and $Z_1^\lambda(t)$,

$$\frac{d}{dt} \begin{pmatrix} N_1^\lambda(t) \\ Z_1^\lambda(t) \end{pmatrix} = \int d^3r g(x') \begin{pmatrix} \hat{e} \cdot \vec{j}_n^\lambda(\vec{r}, t) \\ \hat{e} \cdot \vec{j}_p^\lambda(\vec{r}, t) \end{pmatrix} = \begin{pmatrix} v_n^\lambda(t) \\ v_p^\lambda(t) \end{pmatrix}, \quad (6)$$

with \hat{e} as the unit vector along the symmetry axis with components $\hat{e}_x = \cos\theta$ and $\hat{e}_y = \sin\theta$. In the integrand, we replace the δ function by a smoothing function $\delta(x') \rightarrow g(x')$ in terms of a Gaussian $g(x) = (1/\kappa\sqrt{2\pi}) \exp(-x^2/2\kappa^2)$ with dispersion κ . The Gaussian behaves almost like δ function for sufficiently small κ . In the numerical calculations dispersion of the Gaussian is taken in the order of the lattice side $\kappa = 1.0$ fm. The right-hand side of Eq. (6) defines the fluctuating drift coefficients $v_\alpha^\lambda(t)$ for the neutrons and the protons. There are two different sources for fluctuations of the drift coefficients: (i) fluctuations due to different set of wave functions in each event λ . This part of the fluctuations can be approximately described in terms of the fluctuating macroscopic variables as $v_\alpha^\lambda(t) \rightarrow v_\alpha[N_1^\lambda(t), Z_1^\lambda(t)]$, and (ii) fluctuations introduced by the stochastic part $\delta\rho_{ji}^\lambda = \rho_{ji}^\lambda - \delta_{ji}n_j$ of the density matrix at the initial state. In this work, we consider small amplitude fluctuations, and linearize the Langevin Eq. (6) around the mean values of the macroscopic variables $\delta N_1^\lambda = N_1^\lambda - \bar{N}_1$ and $\delta Z_1^\lambda = Z_1^\lambda - \bar{Z}_1$. The mean values $\bar{N}_1 = \bar{N}_1^\lambda$ and $\bar{Z}_1 = \bar{Z}_1^\lambda$ are determined by the mean-field description of the TDHF approach. Tables I and II show the results of the TDHF calculations for the mean values for a set of observable quantities in the collisions of $^{238}\text{U} + ^{238}\text{U}$ system at $E_{c.m.} = 833$ MeV for the range initial orbital angular momentum $\ell = (100 - 460)\hbar$.

TABLE I. Result of TDHF calculations for tip-tip collisions of $^{238}\text{U} + ^{238}\text{U}$ system at $E_{c.m.} = 833$ MeV for final values of mass and charge of the projectilelike (A_1^f, Z_1^f) and targetlike fragments (A_2^f, Z_2^f), final orbital angular momentum ℓ_f , total kinetic energy (TKE), total excitation energy E^* , center of mass angle $\theta_{c.m.}$, and laboratory scattering angles ($\theta_1^{\text{lab}}, \theta_2^{\text{lab}}$) for a set initial orbital angular momentum ℓ_i .

ℓ_i (\hbar)	A_1^f	Z_1^f	A_2^f	Z_2^f	ℓ_f (\hbar)	TKE (MeV)	E^* (MeV)	$\theta_{c.m.}$ (deg)	θ_1^{lab} (deg)	θ_2^{lab} (deg)
100	238	92.0	238	92.0	73.4	527	306	158	48.3	9.55
120	238	92.0	238	92.0	95.4	514	319	154	49.6	11.5
140	238	92.0	238	92.0	114	505	328	149	50.4	13.6
160	238	92.0	238	92.0	132	521	312	149	51.7	13.7
180	238	92.0	238	92.0	153	510	323	138	51.3	18.5
200	238	92.3	238	91.7	172	515	317	132	50.8	20.9
220	238	92.0	238	92.0	177	525	318	129	50.4	22.4
240	238	92.0	238	92.0	182	552	281	126	51.6	24.1
260	238	91.6	238	92.4	185	577	256	123	52.2	25.6
280	238	92.0	238	92.0	189	595	238	120	51.6	27.4
300	238	92.0	238	92.0	201	616	217	116	51.2	29.3
320	238	92.0	238	92.0	225	625	208	113	50.1	31.0
340	238	92.0	238	92.0	245	645	188	109	49.5	32.8
360	238	92.0	238	92.0	271	654	179	106	48.3	34.6
380	238	92.0	238	92.0	333	714	119	101	47.8	37.7
400	238	92.0	238	92.0	374	751	82.3	98.4	47.5	39.5
420	238	92.0	238	92.0	429	797	35.9	96.2	47.4	41.4
440	238	92.0	238	92.0	439	785	48.1	93.4	45.8	42.5
460	238	92.0	238	92.0	491	819	14.1	91.4	45.5	44.1

The fluctuations evolve according to the linearized coupled Langevin equations,

$$\frac{d}{dt} \begin{pmatrix} \delta Z_1^\lambda \\ \delta N_1^\lambda \end{pmatrix} = \begin{pmatrix} \frac{\partial v_p}{\partial Z_1} (Z_1^\lambda - \bar{Z}_1) + \frac{\partial v_p}{\partial N_1} (N_1^\lambda - \bar{N}_1) \\ \frac{\partial v_n}{\partial Z_1} (Z_1^\lambda - \bar{Z}_1) + \frac{\partial v_n}{\partial N_1} (N_1^\lambda - \bar{N}_1) \end{pmatrix} + \begin{pmatrix} \delta v_p^\lambda(t) \\ \delta v_n^\lambda(t) \end{pmatrix}, \quad (7)$$

where the derivatives of drift coefficients are evaluated at the mean values \bar{N}_1 and \bar{Z}_1 . The linear limit provides a good approximation for small amplitude fluctuations and it becomes even better if the driving potential energy has nearly harmonic behavior around the mean values. The stochastic part $\delta v_\alpha^\lambda(t)$ of drift coefficients given by,

$$\delta v_\alpha^\lambda(t) = \frac{\hbar}{m} \sum_{ij \in \alpha} \int d^3r g(x') \text{Im}(\Phi_j^{*\alpha}(\vec{r}, t) \hat{e} \cdot \vec{\nabla} \Phi_i^\alpha(\vec{r}, t) \delta\rho_{ji}^\lambda). \quad (8)$$

According to the basic postulate of the SMF approach the stochastic elements of the initial density matrix $\delta\rho_{ji}^\lambda$ are specified in terms of uncorrelated distributions, then it follows that the stochastic part of the neutron and proton drift coefficients $\delta v_\alpha^\lambda(t)$ are determined by uncorrelated Gaussian distributions with variances discussed in the following section.

TABLE II. Same as Table I for side-side collisions.

ℓ_i (\hbar)	A_1^f	Z_1^f	A_2^f	Z_2^f	ℓ_f (\hbar)	TKE (MeV)	E^* (MeV)	$\theta_{c.m.}$ (deg)	θ_1^{lab} (deg)	θ_2^{lab} (deg)
100	238	92.3	238	91.7	71.3	658	173	154	62.3	12.5
120	238	92.0	238	92.0	86.5	660	173	149	62.7	14.4
140	238	92.0	238	92.0	99.2	660	173	145	62.0	16.5
160	238	92.0	238	92.0	116	668	165	140	61.3	19.0
180	238	92.0	238	92.0	140	659	174	134	59.3	21.2
200	238	92.1	238	91.9	164	666	167	129	57.8	23.9
220	238	92.0	238	92.0	184	673	160	125	57.6	26.0
240	238	92.0	238	92.0	196	673	160	122	55.5	27.4
260	238	92.0	238	92.0	214	682	214	119	52.2	28.2
280	238	92.0	238	92.0	234	692	141	115	53.4	30.7
300	238	92.0	238	92.0	258	699	134	112	52.1	32.5
320	238	92.0	238	92.0	282	705	128	108	50.8	34.2
340	238	92.0	238	92.0	302	713	120	105	49.8	35.6
360	238	92.0	238	92.0	318	723	110	103	49.1	36.8
380	238	92.0	238	92.0	333	736	96.6	102	48.6	37.8
400	238	92.0	238	92.0	331	751	81.7	99.7	48.1	38.9
420	238	92.0	238	92.0	373	768	65.0	97.8	47.6	40.1
440	238	92.0	238	92.0	393	785	47.6	96.2	47.2	41.2
460	238	92.0	238	92.0	410	802	31.4	94.9	46.9	42.1

III. MASS AND CHARGE DISTRIBUTIONS OF THE PRIMARY FRAGMENTS

A. Quantal diffusion coefficients of neutrons and protons

It is well known that Langevin equation for a macroscopic variable is equivalent to the Fokker-Planck equation for the distribution function of the macroscopic variable and the solution is given by a single Gaussian function [48]. When there are two coupled Langevin equations, as we have it in Eq. (7), the solution of the Fokker-Planck equation for the distribution function $P(N, Z)$ of fragments with neutron and proton numbers (N, Z) is specified by a correlated Gaussian function for each value of the initial orbital angular momentum ℓ ,

$$P(N, Z) = \frac{1}{2\pi\sigma_{NN}\sigma_{ZZ}\sqrt{1-\rho^2}} \exp[-C(N, Z)]. \quad (9)$$

Here the exponent $C(N, Z)$ is given by

$$C(N, Z) = \frac{1}{2(1-\rho^2)} \left[\left(\frac{Z-\bar{Z}}{\sigma_{ZZ}} \right)^2 - 2\rho \left(\frac{Z-\bar{Z}}{\sigma_{ZZ}} \right) \left(\frac{N-\bar{N}}{\sigma_{NN}} \right) + \left(\frac{N-\bar{N}}{\sigma_{NN}} \right)^2 \right], \quad (10)$$

with the correlation coefficient $\rho = \sigma_{NZ}^2/\sigma_{ZZ}\sigma_{NN}$. In this expression \bar{N} and \bar{Z} are the mean values the neutron and the proton numbers of fragments for each angular momentum determined by the TDHF calculations, and σ_{NN} , σ_{ZZ} , and σ_{NZ} denote the neutron, proton, and mixed dispersions, respectively. Multiplying both sides in Eq. (7) by δN_1^λ and δZ_1^λ and carrying out ensemble averaging, we obtain a couple set of equations for the neutron $\sigma_{NN}^2 = \overline{\delta N_1^\lambda \delta N_1^\lambda}$, the proton $\sigma_{ZZ}^2 =$

$\overline{\delta Z_1^\lambda \delta Z_1^\lambda}$ and the mixed variances $\sigma_{NZ}^2 = \overline{\delta N_1^\lambda \delta Z_1^\lambda}$, where bar indicates the ensemble averaging [49,50],

$$\frac{\partial}{\partial t} \sigma_{NN}^2 = 2 \frac{\partial v_n}{\partial N_1} \sigma_{NN}^2 + 2 \frac{\partial v_n}{\partial Z_1} \sigma_{NZ}^2 + 2D_{NN}, \quad (11)$$

$$\frac{\partial}{\partial t} \sigma_{ZZ}^2 = 2 \frac{\partial v_p}{\partial Z_1} \sigma_{ZZ}^2 + 2 \frac{\partial v_p}{\partial N_1} \sigma_{NZ}^2 + 2D_{ZZ}, \quad (12)$$

and

$$\frac{\partial}{\partial t} \sigma_{NZ}^2 = \frac{\partial v_p}{\partial N_1} \sigma_{NN}^2 + \frac{\partial v_n}{\partial Z_1} \sigma_{ZZ}^2 + \sigma_{NZ}^2 \left(\frac{\partial v_p}{\partial Z_1} + \frac{\partial v_n}{\partial N_1} \right). \quad (13)$$

In these expressions D_{NN} and D_{ZZ} denote the neutron and proton quantal diffusion coefficients, which are discussed below. The expression of the diffusion coefficients of for neutron and proton transfers are determined by the autocorrelation functions of the stochastic part of the drift coefficients as

$$\int_0^t dt' \overline{\delta v_\alpha^\lambda(t) \delta v_\alpha^\lambda(t')} = D_{\alpha\alpha}(t). \quad (14)$$

We can calculate the ensemble averaging by employing the basic postulate of the SMF approach given by Eq. (3). We refer the reader to Refs. [39,40] in which a detailed description of the autocorrelation functions are presented. Here, for completeness of the presentation, we give the results for the quantal expression of the proton and the neutron diffusion coefficients,

$$D_{\alpha\alpha}(t) = \int_0^t d\tau \int d^3r \overline{\tilde{g}(x')} [G_T(\tau) J_{\perp,\alpha}^T(\vec{r}, t - \tau/2) + G_P(\tau) J_{\perp,\alpha}^P(\vec{r}, t - \tau/2)] - \int_0^t d\tau \operatorname{Re} \left(\sum_{h' \in P, h \in T} A_{h'h}^\alpha(t) A_{h'h}^{*\alpha}(t - \tau) + \sum_{h' \in T, h \in P} A_{h'h}^\alpha(t) A_{h'h}^{*\alpha}(t - \tau) \right). \quad (15)$$

Here $J_{\perp,\alpha}^T(\vec{r}, t - \tau/2)$ represents the sum of the magnitude of current densities perpendicular to the window due to the hole wave functions originating from target,

$$J_{\perp,\alpha}^T(\vec{r}, t - \tau/2) = \frac{\hbar}{m} \sum_{h \in T} |\operatorname{Im}[\Phi_h^{*\alpha}(\vec{r}, t - \tau/2) \times (\hat{e} \cdot \vec{\nabla} \Phi_h^\alpha(\vec{r}, t - \tau/2))]|. \quad (16)$$

and $J_{\perp,\alpha}^P(\vec{r}, t - \tau/2)$ is given by a similar expression in terms of the hole wave functions originating from the projectile. We observe that there is a close analogy between the quantal expression and the diffusion coefficient in a random walk problem [37,38]. The first line in the quantal expression gives the sum of the nucleon currents across the window from the targetlike fragment to the projectilelike fragment and from the projectilelike fragment to the targetlike fragment, which is integrated over the memory. This is analogous to the random walk problem, in which the diffusion coefficient is given by the sum of the rate for the forward and backward steps. The second line in the quantal diffusion expression stands for the

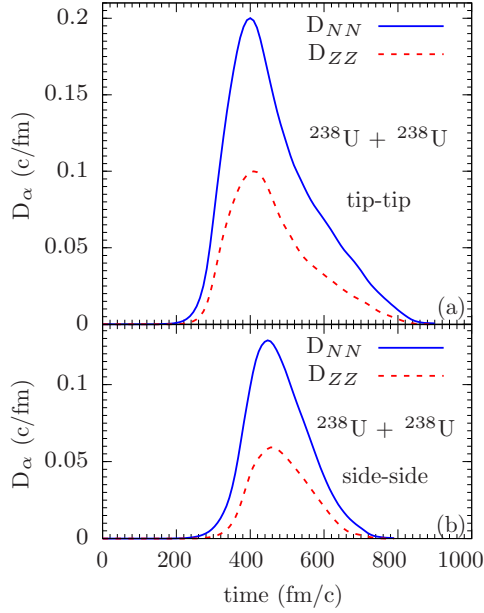


FIG. 2. Neutron and proton diffusion coefficients as a function of time in the $^{238}\text{U} + ^{238}\text{U}$ collisions at $E_{\text{c.m.}} = 833$ MeV with the initial orbital angular momentum $\ell = 300\hbar$ at (a) tip-tip geometry and (b) side-side geometry.

Pauli blocking effects in nucleon transfer mechanism, which does not have a classical counterpart. The quantities in the Pauli blocking factors are determined by

$$A_{h'h}^{\alpha}(t) = \frac{\hbar}{2m} \int d^3r g(x') (\Phi_{h'}^{*\alpha}(\vec{r}, t) \hat{e} \cdot \vec{\nabla} \Phi_h^{\alpha}(\vec{r}, t) - \Phi_h^{\alpha}(\vec{r}, t) \hat{e} \cdot \vec{\nabla} \Phi_{h'}^{*\alpha}(\vec{r}, t)). \quad (17)$$

The memory kernels $G_T(\tau)$ in Eq. (15) are given by

$$G_T(\tau) = \frac{1}{\sqrt{4\pi}} \frac{1}{\tau_T} \exp[-(\tau/2\tau_T)^2] \quad (18)$$

with the memory time determined by the average flow velocity u_T of the target nucleons across the window according to $\tau_T = \kappa/|u_T(t)|$, and $G_p(\tau)$ is given by a similar expression. In a previous work [40], we estimated the memory time to be about $\tau_T = \tau_p \approx 25$ fm/c, which is much shorter than the contact time of about 600 fm/c. As a result the memory effect is not important in diffusion coefficients. We note that the quantal diffusion coefficients are entirely determined in terms of the occupied single-particle wave functions of the TDHF solutions. According to the nonequilibrium fluctuation-dissipation theorem, the fluctuation properties of the relevant macroscopic variables must be related to the mean properties. Consequently, the evaluation of the diffusion coefficients in terms of the mean-field properties is consistent with the fluctuation-dissipation theorem. Figure 2 shows neutron and proton diffusion coefficients for the $^{238}\text{U} + ^{238}\text{U}$ system at $E_{\text{c.m.}} = 833$ MeV with the initial orbital angular momentum $\ell = 300\hbar$, for the tip-tip [Fig. 2(a)] and the side-side [Fig. 2(b)] geometries as function of time.

Dispersions are determined from the solutions of the coupled differential Eqs. (11)–(13) in which the diffusion coef-

ficients provide source for development of the fluctuations. In addition to the diffusion coefficients, we also need to determine the derivatives of the drift coefficients with respect to the macroscopic variables (N_1, Z_1). In order to determine these derivatives, the Einstein's relations in the overdamped limit provide a possible approach. According to the Einstein relation, drift coefficients are determined by the derivatives of the potential energy surface in the (N, Z) plane,

$$v_n(t) = -\frac{D_{NN}}{T^*} \frac{\partial}{\partial N_1} U(N_1, Z_1) \\ v_p(t) = -\frac{D_{ZZ}}{T^*} \frac{\partial}{\partial Z_1} U(N_1, Z_1), \quad (19)$$

where T^* indicates effective temperature of the system. Because of the analytical structure, we can immediately take derivatives of the drift coefficients. Since $^{238}\text{U} + ^{238}\text{U}$ is a symmetric system, the equilibrium state in the potential energy surface is located at the initial position with $N_1 \rightarrow N_0 = 146$ and $Z_1 \rightarrow Z_0 = 92$. When fluctuations are not too far from the equilibrium point, we can parametrize the potential energy around the equilibrium in terms of two parabolic forms as given by Eq. (A1) in Appendix A [50]. One of the parabolic forms extend along the bottom of the β stability line, which is referred to as the isoscalar path. The second parabolic form extends towards the perpendicular direction to the isoscalar path, which is referred to as the isovector path. In order to specify the derivatives of the drift coefficients, we need to determine the reduced curvature parameters α and β of these parabolic potential energy surfaces. Since the symmetric collisions do not exhibit drift in neutron or proton numbers, it is not possible to specify the reduced curvature parameters from the mean trajectory information of the symmetric collisions. As discussed in Appendix A, we can estimate the isovector curvature α parameter from the central collision of the neighboring $^{236}\text{Ra}_{148} + ^{240}\text{Cm}_{144}$ system at $E_{\text{c.m.}} = 833$ MeV. As seen from the drift path of this system in Fig. 7, the system follows the isovector path closely and reaches the charge equilibrium rather rapidly during a time interval of $\Delta t \approx 150$ fm/c. The isovector drift path is suitable to estimate the average value of the isovector curvature parameters and we find $\alpha \approx 0.13$. After reaching the equilibrium in charge asymmetry rather rapidly, the system spends a long time in the vicinity of $^{238}\text{U} + ^{238}\text{U}$ by following a curvy path due to complex quantal effect due to shell structure. Eventually, the system has a tendency to evolve toward asymmetry direction along the isoscalar path, i.e., along the β stability line. It appears that the $^{238}\text{U} + ^{238}\text{U}$ system is located at an unstable state on the β stability line with a small and negative curvature parameter β in the isoscalar direction. It is not possible to provide reasonable estimation for this parameter from the drift path of the $^{236}\text{Ra}_{148} + ^{240}\text{Cm}_{144}$ system in Fig. 8 beyond the equilibrium state at ($N_1 = 146, Z_1 = 92$). With a negative curvature parameter in the isoscalar direction, the system may exhibit broad diffusion along the β stability line. In order obtain a reasonable value for β , we employ the cross-section data for production of gold isotopes from a previous investigation of the $^{238}\text{U} + ^{238}\text{U}$ system at about the same energy [16]. As discussed in Appendix B, we determine a small negative value

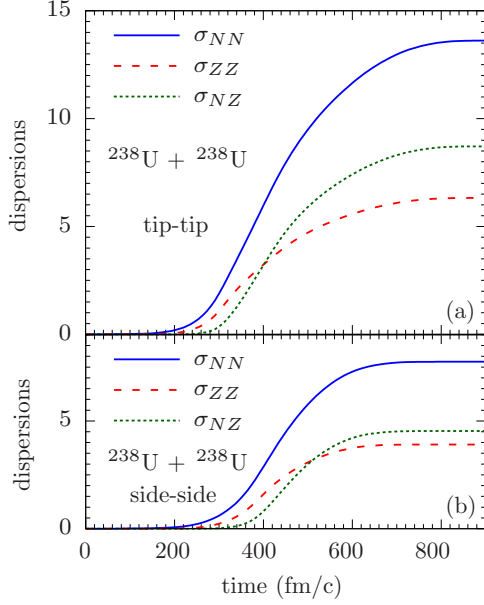


FIG. 3. Neutron, proton, and mixed variance as a function of time in the $^{238}\text{U} + ^{238}\text{U}$ collisions at $E_{\text{c.m.}} = 833$ MeV with the initial orbital angular momentum $\ell = 300\hbar$ at (a) tip-tip geometry and (b) side-side geometry.

of $\beta = -0.02$ for the reduced isoscalar curvature parameter. Using these values for the reduced curvature parameters, we can determine the derivative of the drift coefficients as given in Eqs. (A3)–(A6) and calculate the neutron, the proton and the mixed dispersions from the solution of the differential Eqs. (11)–(13). As an example Fig. 3 shows the neutron, the proton and the mixed dispersions as a function of time in the $^{238}\text{U} + ^{238}\text{U}$ collisions at $E_{\text{c.m.}} = 833$ MeV with the initial orbital angular momentum $\ell = 300\hbar$ at tip-tip geometry and side-side geometry. The asymptotic values of these dispersions for a range of the initial orbital angular momentum $\ell = (100 - 460)\hbar$ in tip-tip and side-side geometries are given in Table III.

B. Cross section of production of primary fragments

We calculate the cross section for production of a primary fragment with neutron and proton numbers (N, Z) using the standard expression,

$$\sigma(N, Z) = \frac{\pi \hbar^2}{2\mu E_{\text{c.m.}}} \sum_{\ell_{\text{min}}}^{\ell_{\text{max}}} (2\ell + 1) P_{\ell}(N, Z). \quad (20)$$

Here, $P_{\ell}(N, Z) = (P_{\ell}^{t-t}(N, Z) + P_{\ell}^{s-s}(N, Z))/2$ denotes the mean value of the probability of producing a primary fragment with neutron and proton numbers (N, Z) in the tip-tip and the side-side collisions with the initial angular momentum ℓ . These probabilities are presented in Eqs. (9)–(10) with the asymptotic values of dispersions given in Table III for tip-tip and side-side collisions. The mean values are equal to their initial values $\bar{N} = 146$, $\bar{Z} = 92$. The range of the summation over the initial angular momentum is taken as $\ell_{\text{min}} = 300$ and $\ell_{\text{max}} = 460$. This angular momentum range

TABLE III. Asymptotic values of the neutron, the proton, and the mixed dispersions in the $^{238}\text{U} + ^{238}\text{U}$ collisions at $E_{\text{c.m.}} = 833$ MeV with the range of orbital angular momentum $\ell = (100-460)\hbar$ at tip-tip geometry (left panel) and side-side geometry (right panel).

$\alpha = 0.13 \quad \beta = -0.02$ (tip-tip)				
$\ell_i(\hbar)$	σ_{NN}	σ_{ZZ}	σ_{NZ}	σ_{AA}
100	21.7	9.91	14.3	31.3
120	22.2	10.2	14.7	28.5
140	23.0	10.6	15.3	29.6
160	22.9	10.4	15.1	29.4
180	23.2	10.5	15.3	29.7
200	22.6	10.2	14.9	32.5
220	21.4	9.68	14.0	30.8
240	19.2	8.76	12.6	27.6
260	14.3	7.97	11.3	25.0
280	15.6	7.15	10.1	22.3
300	13.6	6.32	8.71	19.4
320	13.3	6.23	8.54	19.0
340	11.6	5.53	7.37	16.6
360	10.3	4.99	6.45	14.7
380	6.97	3.53	3.89	9.55
400	5.30	2.79	2.54	6.98
420	3.46	1.72	1.05	4.15
440	3.93	2.07	1.43	4.88
460	2.49	1.14	0.50	2.83
$\alpha = 0.13 \quad \beta = -0.02$ (side-side)				
$\ell_i(\hbar)$	σ_{NN}	σ_{ZZ}	σ_{NZ}	σ_{AA}
100	12.5	5.86	7.95	16.0
120	12.4	5.80	7.85	15.8
140	12.1	5.71	7.69	15.5
160	11.4	5.44	7.18	14.5
180	11.4	5.43	7.19	14.5
200	10.7	5.13	6.68	13.6
220	10.0	4.86	6.22	12.7
240	9.77	4.76	6.05	12.4
260	9.04	4.45	5.51	11.5
280	8.32	4.15	4.97	11.7
300	7.75	3.91	4.53	10.8
320	7.23	3.68	4.13	10.0
340	6.74	3.45	3.73	9.23
360	6.22	3.22	3.30	8.41
380	5.63	2.95	2.81	7.50
400	4.97	2.64	2.28	6.49
420	4.26	2.26	1.70	5.39
440	3.50	1.82	1.12	4.25
460	2.82	1.37	0.68	3.28

corresponds the experimental setup in which the detector is placed at an angular range $\theta = 35^\circ \mp 5^\circ$ in the laboratory frame. Figure 4(a) shows the double cross sections $\sigma(N, Z)$ in the (N, Z) plane. We observe the cross-section distribution extends along the bottom of the β stability and exhibits large dispersion in this direction as a result of the slight negative curvature of the potential energy along the isoscalar direction. We note that the nucleon diffusion along the β stability line is rather sensitive to the magnitude of the reduced isoscalar curvature parameter β . In order to see the effect on the cross

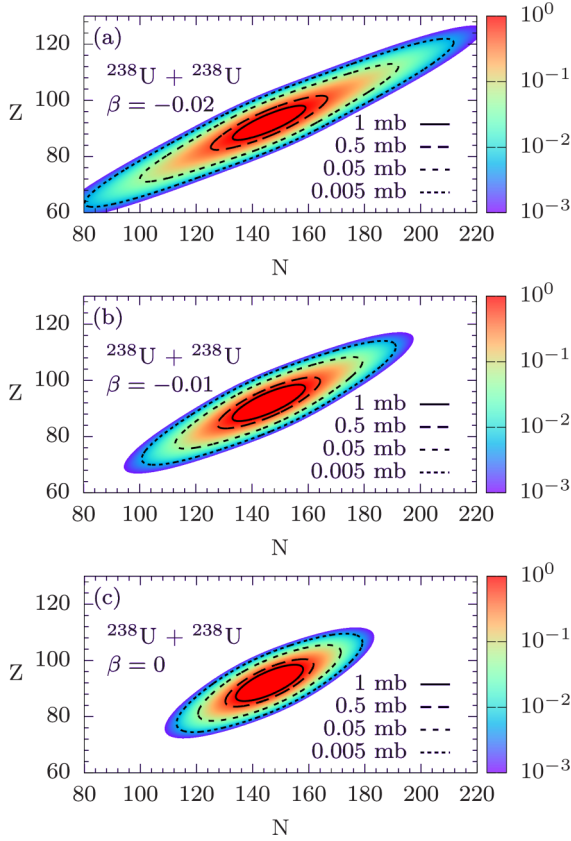


FIG. 4. Double cross sections $\sigma(N, Z)$ for production of primary fragments with neutron numbers N and proton numbers Z in (N, Z) plane in the collisions of $^{238}\text{U} + ^{238}\text{U}$ at $E_{c.m.} = 833$ MeV. Elliptic lines indicate the set of isotopes with equal production cross sections. Calculations were performed with the isoscalar curvature parameters (a) $\beta = -0.02$, (b) $\beta = -0.01$, and (c) $\beta = 0$.

section, we have also calculated the double cross sections with a very small isoscalar curvature parameter, $\beta = -0.01$, and the flat potential energy along the isoscalar direction with $\beta = 0$. The result of these calculations are shown in Figs. 4(b) and 4(c), respectively. We observe that the potential energy in the isoscalar direction has a strong influence on the nucleon diffusion mechanism. As a result, the tail of the cross sections along the isoscalar direction diminishes with decreasing absolute magnitude of the curvature parameter. The cross sections $\sigma(A)$ as a function of the mass numbers of the primary fragments are given by,

$$\sigma(A) = \frac{\pi \hbar^2}{2\mu E_{c.m.}} \sum_{\ell_{\min}}^{\ell_{\max}} (2\ell + 1) P_{\ell}(A). \quad (21)$$

Here $P_{\ell}(A) = (P_{\ell}^{t-t}(A) + P_{\ell}^{s-s}(A))/2$ denotes the mean value of the probability of producing a primary fragment with mass numbers A in the tip-tip and the side-side collisions with the initial angular momentum ℓ . These probabilities are determined by a simple Gaussian function,

$$P(A) = \frac{1}{\sigma_{AA} \sqrt{2\pi}} \exp \left[-\frac{1}{2} \left(\frac{A - \bar{A}}{\sigma_{AA}} \right)^2 \right], \quad (22)$$

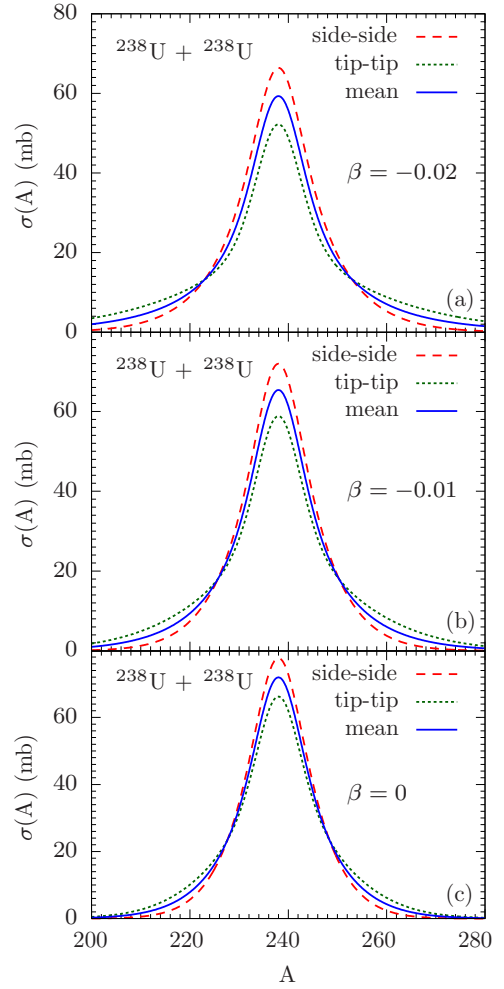


FIG. 5. Cross sections $\sigma(A)$ for production of primary fragments as a function of mass number in the collisions of $^{238}\text{U} + ^{238}\text{U}$ at $E_{c.m.} = 833$ MeV in tip-tip, side-side geometries, and mean values by dashed, dotted, and solid blue lines, respectively. Calculations were performed with the isoscalar curvature parameters (a) $\beta = -0.02$, (b) $\beta = -0.01$, and (c) $\beta = 0$.

where the mass dispersion is determined by $\sigma_{AA}^2 = \sigma_{NN}^2 + \sigma_{ZZ}^2 + 2\sigma_{NZ}^2$ and the mean mass number as $\bar{A} = 238$. Figure 5 shows the cross sections as a function of the mass numbers of the primary fragments in the tip-tip and the side-side geometries and their mean values for the isoscalar curvature parameters $\beta = -0.02$, $\beta = -0.01$, and $\beta = 0$ in Figs. 5(a), 5(b) and 5(c), respectively. We can calculate the cross sections $\sigma(Z)$ of production of the primary fragments as a function of the atomic number using an expression similar to Eq. (21) by employing the Gaussian probability with the dispersion and the mean values as given by $\sigma_{ZZ}(Z)$ and $\bar{Z} = 92$, respectively. Figure 6 shows the cross sections as a function of the atomic numbers of the primary fragments in the tip-tip and the side-side geometries and their mean values for the isoscalar curvature parameters $\beta = -0.02$, $\beta = -0.01$, and $\beta = 0$ in Figs. 6(a), 6(b), and 6(c), respectively. The effect of different isoscalar curvature parameters is important for cross sections lower than 0.1 mb, which is not visible in Figs. 5 and 6.

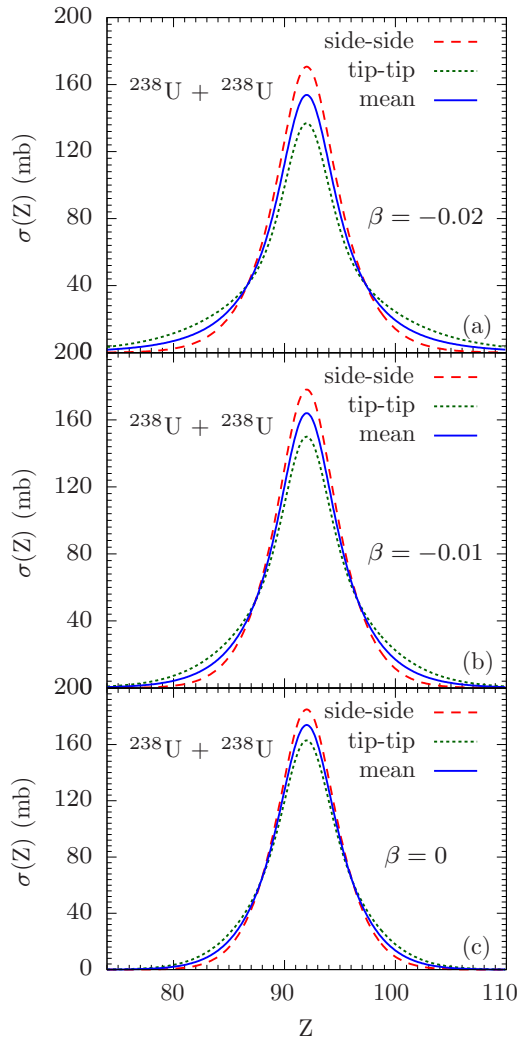


FIG. 6. Cross sections $\sigma(Z)$ for production of primary fragments as a function of mass number in the collisions of $^{238}\text{U} + ^{238}\text{U}$ at $E_{c.m.} = 833$ MeV in tip-tip, side-side geometries, and mean values by dashed, dotted, and solid blue lines, respectively. Calculations were performed with the isoscalar curvature parameters (a) $\beta = -0.02$, (b) $\beta = -0.01$, and (c) $\beta = 0$.

IV. CONCLUSIONS

We have carried out an investigation of mass and charge distributions of the primary fragments produced in the collisions of the $^{238}\text{U} + ^{238}\text{U}$ system at $E_{c.m.} = 833$ MeV. We calculate the probability distributions of the primary fragments by employing the quantal diffusion description. In the quantal diffusion approach, the concepts of the transport theory are merged with the mean-field description of the TDHF with the help of the SMF approach. It is then possible to express the diffusion coefficients of the relevant macroscopic variables in terms of the occupied single-particle wave functions of the TDHF. Since the Langevin equations of the macroscopic variables are equivalent to the Fokker-Planck description for the distribution of the macroscopic variables, under certain conditions, it is possible to give a nearly analytical description for the distribution functions of the macroscopic variables and

the cross sections. In the calculations of the cross sections of production of the primary fragment for each initial angular momentum or equivalently for each impact parameter, we need to determine the mean values of the neutron and proton numbers of the fragments and the neutron, the proton, and the mixed dispersions of the distribution functions. The mean values are determined by the TDHF descriptions. The variances are calculated from the solutions of three coupled differential equations in which diffusion coefficients of neutron and protons act as the source terms. The behavior of the potential energy surface of the di-nuclear complex makes an important effect on the neutron and proton diffusion mechanism. It is possible to determine the curvature parameters of the potential energy in the collisions of asymmetric systems from the drift information with the help of the Einstein's relation in the overdamped limit. Since collisions of the symmetric systems, such as the collisions of $^{238}\text{U} + ^{238}\text{U}$, do not exhibit drift of the neutron and proton degrees of freedom, we need to employ other methods to specify the curvature parameters of the potential energy. In this work, we employ the central collision of a neighboring system $^{236}\text{Ra} + ^{240}\text{Cm}$ at the same bombarding energy. The system initially drifts nearly along the isovector direction and reach the charge equilibrium state rather rapidly. From the isovector drift information, we can estimate the reduced curvature parameter of the potential energy as $\alpha = 0.13$. After reaching the charge equilibration, the system spends a long time in the vicinity of $^{238}\text{U} + ^{238}\text{U}$ state and eventually has a tendency drift along the isoscalar path away from the symmetric state. This behavior indicates the symmetric $^{238}\text{U} + ^{238}\text{U}$ may be located at an unstable equilibrium position with a small negative curvature toward the isoscalar direction. However, from the drift information it is not possible to estimate the isoscalar reduced curvature parameter β . Since the negative curvature may lead to broad diffusion along the β stability line, it is important to determine this curvature parameter accurately. Therefore, we regard the reduced curvature in the isoscalar direction as a parameter and estimate its value with the help of the isotopic cross-section data of gold nucleus from a previous investigation of the $^{238}\text{U} + ^{238}\text{U}$ collisions at about the same energy. In this work, we present calculations for production of the primary fragments with the isovector curvature parameter $\alpha = 0.13$ and the isoscalar curvature parameters $\beta = -0.02$, $\beta = -0.01$, and $\beta = 0$. As a result of growing nucleon diffusion, the tail of the cross sections along the isoscalar direction extends farther with the increasing absolute magnitude of the curvature parameter. The primary fragments are excited and cool down by the deexcitation processes of particle emission, mostly neutrons and by sequential fission of the heavy fragments. Calculations of the secondary cross sections exceed the scope of the present work. We plan to investigate the deexcitation process of the primary fragments in the collisions of $^{238}\text{U} + ^{238}\text{U}$ and calculate the secondary cross sections in a subsequent study.

ACKNOWLEDGMENTS

S.A. gratefully acknowledges the IPN-Orsay and the Middle East Technical University for warm hospitality extended to

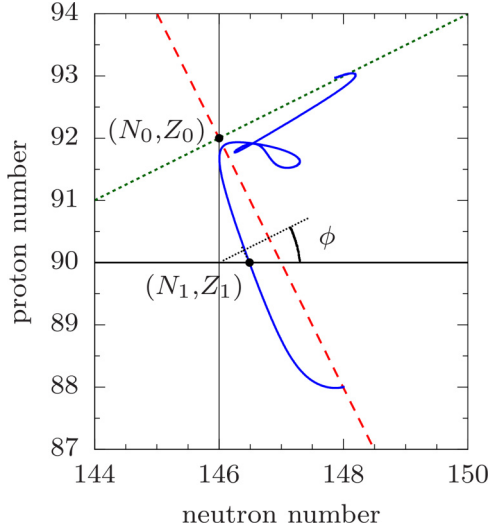


FIG. 7. Drift path of the radiuimlike fragments in the central collisions of the $^{236}\text{Ra} + ^{240}\text{Cm}$ system at $E_{\text{c.m.}} = 833$ MeV (solid blue line) at tip-tip geometry. Dashed green line starting at $(Z_1 = 92, N_1 = 144)$ and the perpendicular dashed red line are the isoscalar and isovector paths, respectively.

him during his visits. S.A. also gratefully acknowledges useful discussions with D. Lacroix, K. Sekizawa, D. Ackermann, and very much thankful to F. Ayik for continuous support and encouragement. This work is supported in part by US DOE Grants No. DE-SC0015513 and No. DE-SC0013847, and in part by TUBITAK Grant No. 117F109.

APPENDIX A: CURVATURE PARAMETERS OF THE POTENTIAL ENERGY

The charge asymmetry of uranium $^{238}\text{U}_{146}$ is $(146 - 92)/(146 + 92) = 0.227$. The dashed green line in Fig. 7 represents the nuclei with nearly equal charge asymmetry $(N - Z)/(N + Z) = 0.22-0.23$. We refer to this line as the isoscalar line, which extends nearly parallel to the lower part of the β stability valley in this region. We refer to the dashed red line as the isovector line, which is perpendicular to the isoscalar path. We parametrize the potential energy surface in the vicinity of the equilibrium $(N_0 = 146, Z_0 = 92)$ in terms of two parabolic forms along the isoscalar and isovector paths as,

$$U(N_1, Z_1) = \frac{1}{2}aR_S^2(N_1, Z_1) + \frac{1}{2}bR_V^2(N_1, Z_1). \quad (\text{A1})$$

The vertical distances R_S and R_V of a point (N_1, Z_1) representing a fragment from the isoscalar and the isovector lines, respectively, are given by,

$$\begin{aligned} R_S &= (Z_0 - Z_1) \cos \phi + (N_1 - N_0) \sin \phi, \\ R_V &= (Z_0 - Z_1) \sin \phi - (N_1 - N_0) \cos \phi. \end{aligned} \quad (\text{A2})$$

According to the Einstein relation in the overdamped limit neutron and proton drift coefficients are related to the driving

potential as,

$$\begin{aligned} v_n &= -\frac{D_{NN}}{T} \frac{\partial U}{\partial N_1} = -\alpha D_{NN} R_S \sin \phi + \beta D_{NN} R_V \cos \phi \\ v_z &= -\frac{D_{ZZ}}{T} \frac{\partial U}{\partial Z_1} = +\alpha D_{ZZ} R_S \cos \phi + \beta D_{ZZ} R_V \sin \phi. \end{aligned}$$

Here, the temperature is absorbed in the reduced curvature parameters as $\alpha = a/T$ and $\beta = b/T$. Because of the analytical form, we can readily calculate the derivatives of the drift coefficients to obtain,

$$\partial v_n(t)/\partial N_1 = -D_{NN}(\beta \cos^2 \phi + \alpha \sin^2 \phi) \quad (\text{A3})$$

$$\partial v_n(t)/\partial Z_1 = +D_{NN}(\alpha - \beta) \cos \phi \sin \phi \quad (\text{A4})$$

$$\partial v_p(t)/\partial Z_1 = -D_{ZZ}(\beta \sin^2 \phi + \alpha \cos^2 \phi) \quad (\text{A5})$$

$$\partial v_p(t)/\partial N_1 = +D_{ZZ}(\alpha - \beta) \cos \phi \sin \phi. \quad (\text{A6})$$

The reduced curvature parameters are determined by the drift and the diffusion coefficients as,

$$\alpha R_S(t) = \frac{v_z(t)}{D_{ZZ}(t)} \cos \phi - \frac{v_n(t)}{D_{NN}(t)} \sin \phi \quad (\text{A7})$$

and

$$\beta R_V(t) = \frac{v_z(t)}{D_{ZZ}(t)} \sin \phi + \frac{v_n(t)}{D_{NN}(t)} \cos \phi. \quad (\text{A8})$$

In collisions of symmetric systems, the drift coefficients vanish and the mean values of the neutron and proton numbers of the fragments are equal to the equilibrium values of the colliding nuclei $\bar{N}_1 = N_0, \bar{Z}_1 = Z_0$. As a result, it is not possible to determine the reduced curvature parameters from the Eq. (A7) and Eq. (A8).

In order to estimate the reduced curvature parameters, we consider the central collision of a neighboring system of $^{236}_{88}\text{Ra}_{148} + ^{240}_{96}\text{Cm}_{144}$ at the same bombarding energy $E_{\text{c.m.}} = 833$ MeV. We consider ^{236}Ra as the projectile. Figure 8 shows the neutron number $N_1(t)$ and the proton number $Z_1(t)$ as a function of time. The blue line in Fig. 7 shows the drift path of the projectilelike fragments in the (N, Z) plane. We observe that the system rapidly evolves toward the equilibrium charge asymmetry of the $^{238}\text{U} + ^{238}\text{U}$ system nearly along the isovector direction from the initial state at point A toward the state at point B. This segment of the drift path is suitable to determine the average value of the reduced isovector curvature as,

$$\alpha \int_{t_A}^{t_B} dt [R_S(t)] = \int_{t_A}^{t_B} dt \left[\frac{v_z(t)}{D_{ZZ}(t)} \cos \phi - \frac{v_n(t)}{D_{NN}(t)} \sin \phi \right], \quad (\text{A9})$$

where $t_A = 250$ fm/c and $t_B = 400$ fm/c as indicated in Fig. 8. In this expression, $D_{ZZ}(t)$ and $D_{NN}(t)$ indicate the proton and neutron diffusion coefficients in the head on collision of $^{236}\text{Ra} + ^{240}\text{Cm}$ system at $E_{\text{c.m.}} = 833$ MeV, which are plotted as a function of time in Fig. 9. We find the reduced isovector curvature parameter as $\alpha = 0.13$. In Fig. 7, after the symmetric state $^{238}\text{U} + ^{238}\text{U}$, because of quantal effects due to shell structure, the TDHF drift path follows a complex pattern for a long time and subsequently appears to drift toward asymmetry along the isoscalar direction. This behavior

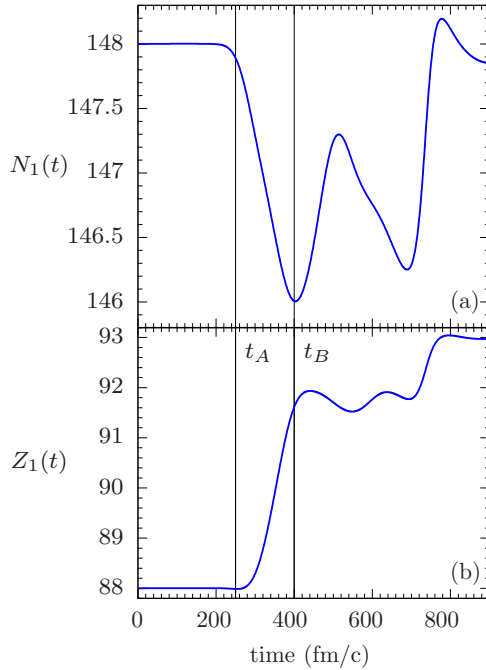


FIG. 8. Neutron $N_1(t)$ and proton $Z_1(t)$ numbers of radium-like fragments as function of time in the central collisions of the $^{236}\text{Ra} + ^{240}\text{Cm}$ system at $E_{\text{c.m.}} = 833$ MeV (solid blue line) at tip-tip geometry.

indicates that the symmetric state is an unstable equilibrium point in the isoscalar direction, i.e., along the β stability line, and the average potential energy has an inverted parabolic shape with a negative curvature parameter. Such potential shape may lead to relative large diffusion along the β stability direction. Unfortunately, the drift segment after the symmetric state until the time at which the fragment separates is not suitable to estimate the average value of the reduced isoscalar curvature parameter β .

APPENDIX B: CURVATURE PARAMETERS ALONG THE β STABILITY

We consider the reduced isoscalar curvature β as a parameter. In order to obtain a reasonable value for β , we employ

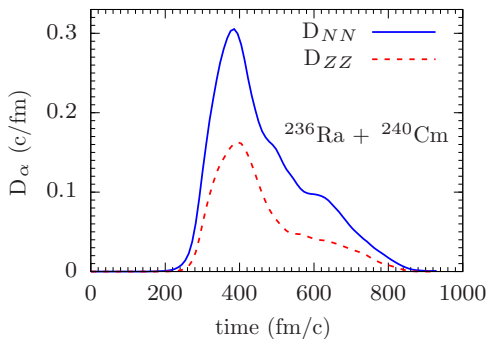


FIG. 9. Neutron and proton diffusion coefficients as function of time in the central collisions of the $^{236}\text{Ra} + ^{240}\text{Cm}$ system at $E_{\text{c.m.}} = 833$ MeV at tip-tip geometry.

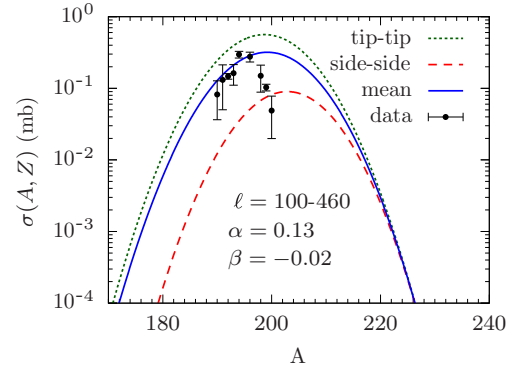


FIG. 10. Cross section of gold $Z = 79$ isotopes averaged over tip-tip and side-side geometries as a function of the mass A numbers in the collisions of $^{238}\text{U} + ^{238}\text{U}$ system at $E_{\text{c.m.}} = 833$ MeV calculated with curvature parameters $\alpha = 0.13$ and $\beta = -0.02$. Solid dots indicate data taken from Ref. [16].

the cross-section data for production of gold isotopes from a previous investigation of the $^{238}\text{U} + ^{238}\text{U}$ system at about the same energy. We calculate the distribution of the cross sections $\sigma(N = A - Z, Z)$ primary gold isotopes with the atomic number $Z = 79$ and mass numbers A using Eq. (20) for the double $\sigma(N, Z)$ cross sections. In order to cover the angular range of the experimental setup in Ref. [16], the range of the angular momentum summation in Eq. (20) is taken as $\ell_{\text{min}} = 100$ and $\ell_{\text{max}} = 460$. Figure 10 shows the cross sections for production of the primary gold isotopes, which are calculated with the reduced isovector curvature $\alpha = 0.13$ and the reduced isoscalar curvature $\beta = -0.02$. The primary gold isotopes are excited and cool down mainly by neutron emissions. In determining the average number of the emitted neutrons, we need to estimate the average excitation energy of these isotopes. The TDHF calculations presented in Tables I and II, do not give accurate information for the total kinetic energy loss (TKEL) in these channels. However, for a rough estimate we can take the results for the initial angular momentum $L = 300\hbar$, which is about the weighted mean value of the angular momentum range. For this angular momentum, the TKEL in the tip-tip and the side-side geometries are 217 MeV and 135 MeV, respectively. For the gold channel $\text{U} + \text{U} \rightarrow \text{Au}(195, 79) + \text{Db}(281, 105)$ the Q_{gg} value is 24.1 MeV. Sharing the TKEL and the Q_{gg} value in proportion to the masses, we find the average excitation energy of the gold isotopes to be 86.8 MeV and 54.0 MeV, in the tip-tip and the side-side geometries, respectively. Assuming one neutron emitted per 10.0 MeV, on the average about 9, 5, and 7 neutrons are emitted in the tip-tip, in the side-side, and in the mean geometry, respectively. In Fig. 10, if we shift the mean gold isotope distribution by seven units to the left, the peak value of the cross sections matches the peak value of the gold data. This indicates $\beta = -0.02$ is a reasonable estimate for the reduced curvature parameter in the isoscalar direction. We note that the calculations overestimate the isotopic width, which most probably is due to the parabolic approximation of the potential energy.

- [1] G. G. Adamian, N. V. Antonenko, and W. Scheid, Characteristics of quasifission products within the dinuclear system model, *Phys. Rev. C* **68**, 034601 (2003).
- [2] V. Zagrebaev and W. Greiner, Shell effects in damped collisions: A new way to superheavies, *J. Phys. G* **34**, 2265 (2007).
- [3] Y. Aritomo, Analysis of dynamical processes using the mass distribution of fission fragments in heavy-ion reactions, *Phys. Rev. C* **80**, 064604 (2009).
- [4] G. G. Adamian, N. V. Antonenko, V. V. Sargsyan, and W. Scheid, Possibility of production of neutron-rich Zn and Ge isotopes in multinucleon transfer reactions at low energies, *Phys. Rev. C* **81**, 024604 (2010).
- [5] J. S. Barrett, W. Loveland, R. Yanez, S. Zhu, A. D. Ayangeakaa, M. P. Carpenter, J. P. Greene, R. V. F. Janssens, T. Lauritsen, E. A. McCutchan, A. A. Sonzogni, C. J. Chiara, J. L. Harker, and W. B. Walters, $^{136}\text{Xe} + ^{208}\text{Pb}$ reaction: A test of models of multinucleon transfer reactions, *Phys. Rev. C* **91**, 064615 (2015).
- [6] H. M. Devaraja, S. Heinz, O. Beliuskina, V. Comas, S. Hofmann, C. Hornung, G. Münzenberg, K. Nishio, D. Ackermann, Y. K. Gambhir, M. Gupta, R. A. Henderson, F. P. Heßberger, J. Khuyagbaatar, B. Kindler, B. Lommel, K. J. Moody, J. Maurer, R. Mann, A. G. Popeko, D. A. Shaughnessy, M. A. Stoyer, and A. V. Yeremin, Observation of new neutron-deficient isotopes with $Z \geq 92$ in multinucleon transfer reactions, *Phys. Lett. B* **748**, 199 (2015).
- [7] K. Zhao, Z. Li, Y. Zhang, N. Wang, Q. Li, C. Shen, Y. Wang, and X. Wu, Production of unknown neutron-rich isotopes in $^{238}\text{U} + ^{238}\text{U}$ collisions at near-barrier energy, *Phys. Rev. C* **94**, 024601 (2016).
- [8] K. Sekizawa and K. Yabana, Time-dependent Hartree-Fock calculations for multinucleon transfer and quasifission processes in the $^{64}\text{Ni} + ^{238}\text{U}$ reaction, *Phys. Rev. C* **93**, 054616 (2016).
- [9] Z.-Q. Feng, Production of neutron-rich isotopes around $N = 126$ in multinucleon transfer reactions, *Phys. Rev. C* **95**, 024615 (2017).
- [10] K. Sekizawa, Enhanced nucleon transfer in tip collisions of $^{238}\text{U} + ^{124}\text{Sn}$, *Phys. Rev. C* **96**, 041601(R) (2017).
- [11] K. Sekizawa, TDHF theory and its extensions for the multinucleon transfer reaction: A mini review, *Front. Phys.* **7**, 20 (2019).
- [12] M.-H. Mun, K. Kwak, G. G. Adamian, and N. V. Antonenko, Possible production of neutron-rich Md isotopes in multinucleon transfer reactions with Cf and Es targets, *Phys. Rev. C* **99**, 054627 (2019).
- [13] V. V. Saiko and A. V. Karpov, Analysis of multinucleon transfer reactions with spherical and statically deformed nuclei using a Langevin-type approach, *Phys. Rev. C* **99**, 014613 (2019).
- [14] X. Jiang and N. Wang, Probing the production mechanism of neutron-rich nuclei in multinucleon transfer reactions, *Phys. Rev. C* **101**, 014604 (2020).
- [15] E. M. Kozulin, E. Vardaci, G. N. Knyazheva, A. A. Bogachev, S. N. Dmitriev, I. M. Itkis, M. G. Itkis, A. G. Knyazev, T. A. Loktev, K. V. Novikov, E. A. Razinkov, O. V. Rudakov, S. V. Smirnov, W. Trzaska, and V. I. Zagrebaev, Mass distributions of the system $^{136}\text{Xe} + ^{208}\text{Pb}$ at laboratory energies around the Coulomb barrier: A candidate reaction for the production of neutron-rich nuclei at $N=126$, *Phys. Rev. C* **86**, 044611 (2012).
- [16] J. V. Kratz, M. Schädel, and H. W. Gäggeler, Reexamining the heavy-ion reactions $^{238}\text{U} + ^{238}\text{U}$ and $^{238}\text{U} + ^{248}\text{Cm}$ and actinide production close to the barrier, *Phys. Rev. C* **88**, 054615 (2013).
- [17] Y. X. Watanabe, Y. H. Kim, S. C. Jeong, Y. Hirayama, N. Imai, H. Ishiyama, H. S. Jung, H. Miyatake, S. Choi, J. S. Song, E. Clement, G. de France, A. Navin, M. Rejmund, C. Schmitt, G. Pollarolo, L. Corradi, E. Fioretto, D. Montanari, M. Niikura, D. Suzuki, H. Nishibata, and J. Takatsu, Pathway for the Production of Neutron-Rich Isotopes Around the $N = 126$ Shell Closure, *Phys. Rev. Lett.* **115**, 172503 (2015).
- [18] V. V. Desai, W. Loveland, K. McCaleb, R. Yanez, G. Lane, S. S. Hota, M. W. Reed, H. Watanabe, S. Zhu, K. Auranen, A. D. Ayangeakaa, M. P. Carpenter, J. P. Greene, F. G. Kondev, D. Seweryniak, R. V. F. Janssens, and P. A. Copp, The $^{136}\text{Xe} + ^{198}\text{Pt}$ reaction: A test of models of multi-nucleon transfer reactions, *Phys. Rev. C* **99**, 044604 (2019).
- [19] V. Zagrebaev and W. Greiner, Production of New Heavy Isotopes in Low-Energy Multinucleon Transfer Reactions, *Phys. Rev. Lett.* **101**, 122701 (2008).
- [20] V. I. Zagrebaev and W. Greiner, Production of heavy and superheavy neutron-rich nuclei in transfer reactions, *Phys. Rev. C* **83**, 044618 (2011).
- [21] V. I. Zagrebaev, A. V. Karpov, and W. Greiner, Possibilities for synthesis of new isotopes of superheavy elements in fusion reactions, *Phys. Rev. C* **85**, 014608 (2012).
- [22] A. V. Karpov and V. V. Saiko, Modeling near-barrier collisions of heavy ions based on a Langevin-type approach, *Phys. Rev. C* **96**, 024618 (2017).
- [23] C. Simenel, Nuclear quantum many-body dynamics, *Eur. Phys. J. A* **48**, 152 (2012).
- [24] T. Nakatsukasa, K. Matsuyanagi, M. Matsuo, and K. Yabana, Time-dependent density-functional description of nuclear dynamics, *Rev. Mod. Phys.* **88**, 045004 (2016).
- [25] V. E. Oberacker, A. S. Umar, and C. Simenel, Dissipative dynamics in quasifission, *Phys. Rev. C* **90**, 054605 (2014).
- [26] V. E. Oberacker, A. S. Umar, J. A. Maruhn, and P.-G. Reinhard, Microscopic study of the $^{132,124}\text{Sn} + ^{96}\text{Zr}$ reactions: Dynamic excitation energy, energy-dependent heavy-ion potential, and capture cross section, *Phys. Rev. C* **82**, 034603 (2010).
- [27] A. S. Umar, V. E. Oberacker, and C. Simenel, Shape evolution and collective dynamics of quasifission in the time-dependent Hartree-Fock approach, *Phys. Rev. C* **92**, 024621 (2015).
- [28] C. Simenel and A. S. Umar, Heavy-ion collisions and fission dynamics with the time-dependent Hartree-Fock theory and its extensions, *Prog. Part. Nucl. Phys.* **103**, 19 (2018).
- [29] C. Simenel, Particle Transfer Reactions with the Time-Dependent Hartree-Fock Theory Using a Particle Number Projection Technique, *Phys. Rev. Lett.* **105**, 192701 (2010).
- [30] R. Balian and M. Vénéroni, Fluctuations in a time-dependent mean-field approach, *Phys. Lett. B* **136**, 301 (1984).
- [31] R. Balian and M. Vénéroni, Time-dependent variational principle for the expectation value of an observable: Mean-field applications, *Ann. Phys. (NY)* **164**, 334 (1985).
- [32] J. M. A. Broomfield and P. D. Stevenson, Mass dispersions from giant dipole resonances using the Balian-Vénéroni variational approach, *J. Phys. G* **35**, 095102 (2008).
- [33] E. Williams, K. Sekizawa, D. J. Hinde, C. Simenel, M. Dasgupta, I. P. Carter, K. J. Cook, D. Y. Jeung, S. D. McNeil, C. S. Palshetkar, D. C. Rafferty, K. Ramachandran, and A. Wakhle, Exploring Zeptosecond Quantum Equilibration Dynamics: From Deep-Inelastic to Fusion-Fission Outcomes in $^{58}\text{Ni} + ^{60}\text{Ni}$ Reactions, *Phys. Rev. Lett.* **120**, 022501 (2018).

- [34] K. Godbey and A. S. Umar, Quasifission dynamics in microscopic theories, *Front. Phys.* **8**, 40 (2020).
- [35] S. Ayik, A stochastic mean-field approach for nuclear dynamics, *Phys. Lett. B* **658**, 174 (2008).
- [36] D. Lacroix and S. Ayik, Stochastic quantum dynamics beyond mean field, *Eur. Phys. J. A* **50**, 95 (2014).
- [37] C. W. Gardiner, *Quantum Noise* (Springer-Verlag, Berlin, 1991).
- [38] U. Weiss, *Quantum Dissipative Systems*, 2nd ed. (World Scientific, Singapore, 1999).
- [39] S. Ayik, B. Yilmaz, O. Yilmaz, A. S. Umar, and G. Turan, Multinucleon transfer in central collisions of $^{238}\text{U} + ^{238}\text{U}$, *Phys. Rev. C* **96**, 024611 (2017).
- [40] S. Ayik, B. Yilmaz, O. Yilmaz, and A. S. Umar, Quantal diffusion description of multinucleon transfers in heavy-ion collisions, *Phys. Rev. C* **97**, 054618 (2018).
- [41] B. Yilmaz, S. Ayik, O. Yilmaz, and A. S. Umar, Multinucleon transfer in $^{58}\text{Ni} + ^{60}\text{Ni}$ and $^{60}\text{Ni} + ^{60}\text{Ni}$ in a stochastic mean-field approach, *Phys. Rev. C* **98**, 034604 (2018).
- [42] S. Ayik, B. Yilmaz, O. Yilmaz, and A. S. Umar, Quantal diffusion approach for multinucleon transfers in Xe+ Pb collisions, *Phys. Rev. C* **100**, 014609 (2019).
- [43] K. Sekizawa and S. Ayik, Quantal diffusion approach for multinucleon transfer processes in the $58,64\text{Ni}+208\text{Pb}$ reactions: Toward the production of unknown neutron-rich nuclei, *Phys. Rev. C* **102**, 014620 (2020).
- [44] O. Yilmaz, G. Turan, and B. Yilmaz, Quasi-fission and fusion-fission reactions in $^{48}\text{Ca} + ^{208}\text{Pb}$ collisions at $E_{\text{c.m.}} = 190$ MeV, *Eur. Phys. J. A* **56**, 37 (2020).
- [45] A. S. Umar, M. R. Strayer, J. S. Wu, D. J. Dean, and M. C. Güçlü, Nuclear Hartree-Fock calculations with splines, *Phys. Rev. C* **44**, 2512 (1991).
- [46] A. S. Umar and V. E. Oberacker, Three-dimensional unrestricted time-dependent Hartree-Fock fusion calculations using the full Skyrme interaction, *Phys. Rev. C* **73**, 054607 (2006).
- [47] K.-H. Kim, T. Otsuka, and P. Bonche, Three-dimensional TDHF calculations for reactions of unstable nuclei, *J. Phys. G* **23**, 1267 (1997).
- [48] H. Risken and T. Frank, *The Fokker-Planck Equation* (Springer-Verlag, Berlin, 1996).
- [49] W. U. Schröder, J. R. Huizenga, and J. Randrup, Correlated mass and charge transport induced by statistical nucleon exchange in damped nuclear reactions, *Phys. Lett. B* **98**, 355 (1981).
- [50] A. C. Merchant and W. Nörenberg, Microscopic transport theory of heavy-ion collisions, *Z. Phys. A* **308**, 315 (1982).